An elliptic blending differential flux model for natural, mixed and forced convection

F. Dehoux, Sofiane Benhamadouche, Remi Manceau

An elliptic blending differential flux model for natural, mixed and forced convection

F. Dehoux[a,b], S. Benhamadouche[a], R. Manceau[b,c,*]

[a] *EDF R&D, MFEE Dept., 06 quai Watier, 78400 Chatou, France*
[b] *Institute Pprime, Dept. Fluid flow, heat transfer and combustion, CNRS-Univ. of Poitiers-ENSMA, SP2MI, téléport 2, 11 bd Marie et Pierre Curie, BP 30179, 86962 Futuroscope Chasseneuil Cedex, France*
[c] *Dept. of mathematics and applied mathematics, Inria-Cagire group, CNRS-university of Pau, IPRA, avenue de l'université, BP115, 64013 Pau Cedex, France*

Abstract

Several modifications are introduced to the Elliptic Blending Differential Flux Model proposed by Shin et al. (2008) to account for the influence of wall blockage on the turbulent heat flux. These modifications are introduced in order to reproduce, in association with the most recent version of the EB-RSM, the full range of regimes, from forced to natural convection, without any case-specific modification. The interest of the new model is demonstrated using analytical arguments, *a priori* tests and computations in channel flows in the different convection regimes, as well as in a differentially heated cavity.

1. Introduction

Many industrial applications involving heat or mass transfer phenomena, in particular in the field of energy production, are still treated with linear eddy-viscosity models and the Simple Gradient Diffusion Hypothesis (SGDH) to model the turbulent heat fluxes. Within this class of models, one of the most successful approaches in forced convection flows (e.g., Parneix et al., 1998; Manceau et al., 2000; Sveningsson and Davidson, 2005; Billard and Laurence, 2012) is the elliptic relaxation concept, under the form of its eddy-viscosity version, the V2F model, originally developed by Durbin (1991), or one of its stabilized formulations (Hanjalić et al., 2004; Laurence et al., 2005), combined to a SGDH approach with a constant turbulent Prandtl number. For buoyant flows, a step further in the sophistication of the elliptic relaxation models was made by Kenjereš et al. (2005), who introduced an algebraic flux model (AFM) with a buoyancy-extended V2F model. However, it is generally admitted that the Reynolds-stress models are desirable (Hanjalić and Launder, 2011) for mixed and natural convection, due to the presence of significant anisotropic phenomena.

In the last few years, the Elliptic Blending Reynolds-Stress Model (EB-RSM, Manceau and Hanjalić, 2002), has emerged as a numerically robust alternative to the elliptic relaxation concept, in particular for isothermal and forced convection applications (e.g., Thielen et al., 2005; Borello et al., 2005; Viti et al., 2007; Billard et al., 2011). The Generalized Gradient Diffusion Hypothesis (GGDH, Daly and Harlow, 1970) proved sufficient to model the turbulent heat fluxes in the absence of buoyancy, due to the correct reproduction of turbulence anisotropy in the near-wall region by the EB-RSM. For the mixed and natural convection regimes, transposing the model of Manceau and Hanjalić (2002) for the Reynolds stresses into a model for the turbulent heat fluxes, Shin et al. (2008) proposed a differential flux model (DFM) based on the elliptic blending strategy to account for the near-wall region. However, as will be shown in section 4, this model is not fully satisfactory in the natural convection regime, which led Choi and Kim (2008) to modify the coefficients of the EB-RSM in order to improve the predictions, at the expenses of the predictions in forced convection. The present work aims at developing a modified EB-DFM that can be used in association with the most recent version of the EB-RSM (Manceau, 2015) in the full range of regimes, from forced to natural convection, without any case-specific modification.

2. The Elliptic Blending strategy

The Reynolds-stress transport equation reads

$$\frac{\partial \rho \overline{u_i' u_j'}}{\partial t} + \frac{\partial \rho \overline{u_k} \, \overline{u_i' u_j'}}{\partial x_k} = \rho \left(P_{ij} + D_{ij}^{\nu} + D_{ij}^{t} + \phi_{ij}^{*} - \varepsilon_{ij} + G_{ij} \right) \quad (1)$$

where P_{ij}, D_{ij}^{ν}, D_{ij}^{T}, ϕ_{ij}^{*} and ε_{ij} stand for the production, the molecular diffusion, the turbulent diffusion, the velocity-pressure gradient correlation and the dissipation tensors, respectively. $G_{ij} = -g_i \beta \overline{u_j' \theta'} - g_j \beta \overline{u_i' \theta'}$ is the production term arising from buoyancy forces, assuming a linear variation of density with temperature. Note that,

*Corresponding author: remi.manceau@univ-pau.fr

throughout the present paper, the Boussinesq approximation is used, i.e., the density variations are only accounted for in buoyant terms and the velocity field is divergence-free.

In order to account for the effects of wall blockage on turbulence (Manceau, 2015), in the EB-RSM, the difference $\phi^*_{ij} - \varepsilon_{ij}$ is formulated as a blending

$$\phi^*_{ij} - \varepsilon_{ij} = (1-\alpha^3)(\phi^w_{ij} - \varepsilon^w_{ij}) + \alpha^3(\phi^h_{ij} - \varepsilon^h_{ij}), \tag{2}$$

of a quasi-homogeneous model $\phi^h_{ij} - \varepsilon^h_{ij}$ (i.e., a model not valid in the near-wall region and requiring the use of wall functions), herein the SSG model (Speziale et al., 1991); and the near-wall model given by

$$\begin{aligned}\phi^w_{ij} &= -5\frac{\varepsilon}{k}\Bigg[\overline{u'_iu'_k}n_jn_k + \overline{u'_ju'_k}n_in_k \\ &\qquad -\frac{1}{2}\overline{u'_ku'_l}n_kn_l\left(n_in_j+\delta_{ij}\right)\Bigg], \qquad (3)\\ \varepsilon^w_{ij} &= \frac{\overline{u'_iu'_j}}{k}\varepsilon. \qquad (4)\end{aligned}$$

The blending function α^3 is related to the distance-to-the-wall-sensitive function α, solution of the elliptic relaxation equation:

$$\alpha - L^2\nabla^2\alpha = 1, \tag{5}$$

which is zero at the wall (Dirichlet boundary condition) and goes to unity far from the wall. The unit vector $\mathbf{n}$ is a generalization of the notion of wall-normal vector: $\mathbf{n} = \boldsymbol{\nabla}\alpha/\|\boldsymbol{\nabla}\alpha\|$.

The dissipation equation reads

$$\frac{\mathrm{D}\varepsilon}{\mathrm{D}t} = \frac{C'_{\varepsilon_1}P - C_{\varepsilon_2}\varepsilon}{\tau} + \frac{\partial}{\partial x_l}\left(\frac{C_\mu}{\sigma_\varepsilon}\overline{u'_lu'_m}\,\tau\,\frac{\partial\varepsilon}{\partial x_m}\right) + \nu\frac{\partial^2\varepsilon}{\partial x_k\partial x_k}, \tag{6}$$

where τ is Durbin's time scale

$$\tau = \max\left(\frac{k}{\varepsilon}, C_T\sqrt{\frac{\nu}{\varepsilon}}\right). \tag{7}$$

The variable $C'_{\varepsilon 1}$ coefficient

$$C'_{\varepsilon_1} = C_{\varepsilon_1}\left[1 + A_1\left(1-\alpha^3\right)\frac{P}{\varepsilon}\right] \tag{8}$$

is intended to represent the term $P_{\varepsilon 3}$ in the exact ε-equation (Hanjalić and Launder, 2011), which stimulates the production of dissipation in the buffer layer (Mansour et al., 1988). Since the initial proposal of Manceau and Hanjalić (2002), the model has undergone numerous modifications. The full set of equations and coefficients is given in Appendix A. For a justification of the version used in the present work, the reader is referred to Manceau (2015).

For mixed and natural convection, elaborate heat flux models are needed in order to account for buoyancy/turbulence interactions (Hanjalić, 2002). Shin et al. (2008) and Choi and Kim (2008) proposed extensions of the elliptic blending strategy to full differential flux models (DFMs), in order to account for the influence of the wall on the turbulent heat flux. With the objective of avoiding the resolution of additional transport equations, Dehoux et al. (2012) derived an *implicit* algebraic version of such models, called the elliptic-blending algebraic flux model (EB-AFM), which is merely a near-wall extension of the standard AFM (Dol et al., 1997). Recently, Vanpouille et al. (2014) derived an *explicit* algebraic heat flux model using the elliptic blending strategy, and successfully computed buoyant flows in mixed and natural convection regimes.

A DFM consists in closing the Reynolds-averaged temperature equation by solving the transport equation for the turbulent heat flux,

$$\frac{D\rho\,\overline{u'_i\theta'}}{Dt} = \rho\left(P_{i\theta} + G_{i\theta} + \phi^*_{i\theta} - \varepsilon_{i\theta} + D^\nu_{i\theta} + D^t_{i\theta}\right). \tag{9}$$

In this equation, the production terms $P_{i\theta}$ and $G_{i\theta}$ do not require modelling, contrary to the scrambling term $\phi^*_{i\theta}$, the dissipation term $\varepsilon_{i\theta}$ and the turbulent and molecular diffusion terms $D^t_{i\theta}$ and $D^\nu_{i\theta}$. Shin et al. (2008) and Choi and Kim (2008) applied the elliptic blending strategy (see Eq. 2) to the scrambling and dissipation vectors,

$$\begin{aligned}\phi^*_{i\theta} &= \left(1-\alpha^n_\theta\right)\phi^w_{i\theta} + \alpha^n_\theta\phi^h_{i\theta}, \\ \varepsilon_{i\theta} &= \left(1-\alpha^n_\theta\right)\varepsilon^w_{i\theta} + \alpha^n_\theta\varepsilon^h_{i\theta}, \qquad (10)\end{aligned}$$

where $\alpha_\theta = \alpha$ is chosen as the same blending function as used in Eq. (2), and $n = 2$. Similar to the case of the Reynolds stresses, this approach makes possible the extension to the near-wall region of quasi-homogeneous models $\phi^h_{i\theta}$ and $\varepsilon^h_{i\theta}$. Assuming the isotropy of the small scales, $\varepsilon^h_{i\theta} = 0$ is imposed; for the scrambling term $\phi^h_{i\theta}$, the standard quasi-homogeneous model

$$\phi^h_{i\theta} = -C_{1\theta}\frac{1}{\tau}\overline{u'_i\theta'} + C_{2\theta}\overline{u'_j\theta'}\frac{\partial\overline{u_i}}{\partial x_j} + C_{3\theta}\beta g_i\overline{\theta'^2} \tag{11}$$

is used. Shin et al. (2008) and Choi and Kim (2008) used the coefficients proposed by Launder (1988) and Peeters and Henkes (1992), respectively.

In order to satisfy the asymptotic near-wall behaviour of the difference $\phi^w_{i\theta} - \varepsilon^w_{i\theta}$, Shin et al. (2008) showed that the two terms can be written as

$$\phi^w_{i\theta} = -\left[1 + \frac{\gamma_1}{2}\left(1 + \frac{1}{Pr}\right)\right]\frac{1}{\tau}\overline{u'_k\theta'}n_kn_i \tag{12}$$

and

$$\varepsilon_{i\theta} = \frac{1}{2}\left(1 + \frac{1}{Pr}\right)\frac{1}{\tau}\left(\overline{u'_i\theta'} + (1-\gamma_1)\overline{u'_k\theta'}n_kn_i\right). \tag{13}$$

Note that the asymptotic analysis leading to these equations is based on the common assumption that the fluctuations of the wall temperature are negligible due to the thermal inertia of the solid material. The additional complexity due to conjugate heat transfer when the conduction in the solid cannot be neglected (Tiselj et al., 2001; Flageul et al., 2015), or simply due to an imposed heat flux at the wall, is not addressed herein and is left to future work. Here, the difference $\phi^w_{i\theta} - \varepsilon^w_{i\theta}$, and consequently, the results, are independent of the particular value of γ_1,

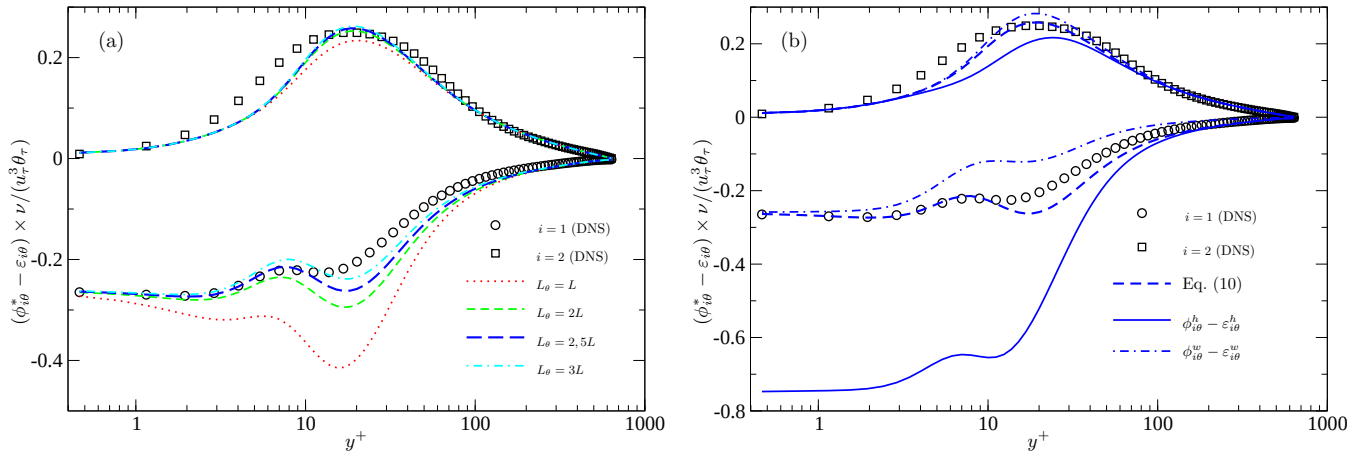

Figure 1: Channel flow in the forced convection regime of Abe et al. (2004) at $Re_\tau = 640$ and $Pr = 0.71$. (a) *A priori test* of the model for $\phi^*_{i\theta} - \varepsilon_{i\theta}$ using different length scales. (b) Comparison of the quasi-homogeneous, near-wall and blended models for $\phi^*_{i\theta} - \varepsilon_{i\theta}$ in the case $L_\theta = 2,5L$. A factor of 4 is applied to $\phi^*_{2\theta} - \varepsilon_{2\theta}$ for clarity.

since only this difference is involved in Eq. (9). Shin et al. (2008) used $\gamma_1 = 1$, whereas, in order to satisfy the individual asymptotic behaviour of $\phi^w_{i\theta}$ and $\varepsilon^w_{i\theta}$, Choi and Kim (2008) used $\gamma_1 = 0$.

Turbulent and molecular diffusion terms are modelled as

$$D^t_{i\theta} = \frac{\partial}{\partial x}\left(C_\theta \overline{u_k' u_l'} \tau \frac{\partial \overline{u_i' \theta'}}{\partial x_l}\right) \tag{14}$$

(Daly and Harlow, 1970) and

$$D^\nu_{i\theta} = \frac{\partial}{\partial x_k}\left(\frac{\kappa + \nu}{2}\frac{\partial \overline{u_i' \theta'}}{\partial x_k} + \gamma_2 n_i n_j \frac{\nu - \kappa}{6}\frac{\partial \overline{u_j' \theta'}}{\partial x_k}\right), \tag{15}$$

respectively. Choi and Kim (2008) and Shin et al. (2008) used $\gamma_2 = 1$ (Shikazono and Kasagi, 1996) and $\gamma_2 = 0$ (Peeters and Henkes, 1992), respectively.

The transport equation for the temperature variance is simply modelled as

$$\frac{\partial \rho \overline{\theta'^2}}{\partial t} + \frac{\partial\left(\rho \overline{u_j}\ \overline{\theta'^2}\right)}{\partial x_j} = \frac{\partial}{\partial x_k}\left[\left(\rho\kappa\delta_{kl} + C_\theta \rho \tau \overline{u_k' u_l'}\right)\frac{\partial \overline{\theta'^2}}{\partial x_l}\right] + \rho P_\theta - \rho\varepsilon_\theta, \tag{16}$$

where P_θ is the exact production term and the dissipation term ε_θ is evaluated as

$$\varepsilon_\theta = \frac{\overline{\theta'^2}}{R}\frac{\varepsilon}{k}, \tag{17}$$

assuming a constant thermal-to-mechanical time-scale ratio R.

3. Modification of the EB-DFM

Although the EB-DFM, as proposed by Shin et al. (2008) and Choi and Kim (2008), is able to satisfactorily reproduce, in association with the EB-RSM, the behaviour of the mechanical and thermal turbulent fields in the near-wall region, the predictions are very sensitive to modelling details, in particular in the natural convection regime, and the present work aims at closely investigating the influence of different terms, more specifically the length scale that drives the migration of the scrambling and dissipation vectors from their near-wall form to their quasi-homogeneous form, and the time scale that enters the dissipation rate and turbulent heat flux equations.

3.1. Length scale

As shown by Dehoux et al. (2012), the smooth transition from the near-wall to the quasi-homogeneous behavior of the source terms in the heat flux transport equation is driven by a length scale L_θ that arises from the modelling of the two-point correlation between the temperature and the Laplacian of the pressure gradient. There is no reason for this length scale to be identical to the length scale L involved in Eq. (5), which is linked to the two-point correlation between the velocity and the Laplacian of the pressure gradient (for details, see Manceau et al., 2001). Assuming that $L_\theta = L$ and, consequently, $\alpha_\theta = \alpha$ in Eq. (10), as proposed by Shin et al. (2008) and Choi and Kim (2008), is thus a questionable hypothesis, that we propose to avoid. Therefore, after Dehoux et al. (2012), we solve an elliptic relaxation equation for α_θ,

$$\alpha_\theta - L_\theta^2 \nabla^2 \alpha_\theta = 1, \tag{18}$$

such that two parameters play an important role in the blending formula (10): the exponent n and the length scale L_θ.

The exponent n in Eq. (10) must be carefully chosen in order to ensure the correct asymptotic behaviour of the difference $\phi^*_{2\theta} - \varepsilon_{2\theta}$ in the transport equation for the wall-normal heat flux, in order to reproduce the wall blockage of this component. Eq. (10) can be recast as

$$\alpha_\theta^n = \frac{(\phi^*_{2\theta} - \varepsilon_{2\theta}) - (\phi^w_{2\theta} - \varepsilon^w_{2\theta})}{(\phi^h_{2\theta} - \varepsilon^h_{2\theta}) - (\phi^w_{2\theta} - \varepsilon^w_{2\theta})}, \tag{19}$$

which can be easily shown to go to zero as $\mathcal{O}(y)$ in the vicinity of the wall. Since Eq. (18), with the boundary condition $\alpha_\theta = 0$ at the wall yields $\alpha_\theta = \mathcal{O}(y)$, $n = 1$ must be chosen in Eq. (10), contrary to the choice $n = 2$ made by Shin et al. (2008) and Choi and Kim (2008) or $n = 3$ made by Dehoux et al. (2012).

Dehoux et al. (2012) showed that the length scale L_θ can be simply modelled as proportional to L,

$$L_\theta = C_L L. \tag{20}$$

However, since we use a different exponent n in Eq. (10), the value of the coefficient C_L must be recalibrated. Fig. 1a shows the influence of the choice of the length scale L_θ, using the DNS database of a channel flow in the forced convection regime at $Re_\tau = 640$ and $Pr = 0.71$ (Abe et al., 2004). It is clearly seen, in particular for the first component (parallel to the wall), that using $L_\theta = L$ is detrimental to the quality of the results. The value $C_L = 2.5$, which yields the best agreement in the vicinity of the wall, is retained. Fig. 1b illustrates the interest of the model given by Eq. (10), by comparing the prediction of $\phi^*_{i\theta} - \varepsilon_{i\theta}$ provided by the quasi-homogeneous model, the near-wall model and the blending of these two models. For the wall-normal component, the quasi-homogeneous and near-wall models are both valid in the viscous sublayer and the log layer, and the improvement is apparent only in the buffer layer. However, the quasi-homogeneous model strongly overestimates the magnitude of the wall-parallel component in the near-wall region, and this behaviour is corrected by the blending with the asymptotically correct near-wall model.

3.2. Time scales

The major modification of the EB-DFM model, as compared with the models proposed by Shin et al. (2008) and Choi and Kim (2008), is concerned with the time scales. Firstly, in the presence of buoyancy effects, an additional term appears in the exact transport equation for the turbulent energy dissipation rate ε (Hanjalić and Launder, 2011),

$$G_\varepsilon = -2\nu\beta g_i \overline{\frac{\partial u_i'}{\partial x_l}\frac{\partial \theta'}{\partial x_l}}. \tag{21}$$

It is usual to model G_ε as analogous to the contribution of buoyancy to the turbulence kinetic energy production $G = G_{ii}/2$, such that

$$P_\varepsilon + G_\varepsilon = C_{\varepsilon 1}\frac{P+G}{\tau}. \tag{22}$$

Since the EB-RSM is a near-wall model, the production term $P_{\varepsilon 3}$ in the exact ε-equation cannot be neglected (Hanjalić and Launder, 2011), and its effect is accounted for by making the $C_{\varepsilon 1}$ coefficient variable (see Eq. 8). However, G_ε is due to buoyancy, while P_ε is a purely mechanical term, such that the variable coefficient $C'_{\varepsilon 1}$ should not be applied to G_ε. Therefore, the model given by Eq. (22), and used by Choi and Kim (2008) and Shin et al. (2008), is modified as

$$P_\varepsilon + G_\varepsilon = C'_{\varepsilon 1}\frac{P}{\tau} + C_{\varepsilon 3}\frac{G}{\tau'}\ . \tag{23}$$

A virtue of the separation of the two contributions is that a specific time scale τ' can be introduced for the term G_ε, which has no reason to be the same as the mechanical time scale τ. In order to investigate how τ' can be modelled, the particular case of homogeneous turbulence is considered, although the conclusions will not be strictly valid in inhomogeneous situations, in particular close to the wall: the subsequent analysis is only intended to provide arguments for the choice of the time scale. For a given direction $\mathbf{e}_\alpha$, introducing the longitudinal two-point correlation function

$$f(r) = \frac{\overline{u'_\alpha(\mathbf{x})\theta'(\mathbf{x}+r\,\mathbf{e}_\alpha)}}{\overline{u'_\alpha(\mathbf{x})\theta'(\mathbf{x})}} \tag{24}$$

and the associated Taylor micro-scale

$$\lambda'^2 = -\frac{1}{2}\left.\frac{\partial^2 f}{\partial r^2}\right|_{r=0}, \tag{25}$$

it is simple algebra to show that

$$\overline{\frac{\partial u'_\alpha}{\partial x_\alpha}\frac{\partial \theta'}{\partial x_\alpha}} = 2\frac{\overline{u'_\alpha\theta'}}{\lambda'^2} \tag{26}$$

(without summation over Greek indices), such that, if the dissipative scales are nearly isotropic, we have

$$G_\varepsilon = -6\beta\nu g_i\frac{\overline{u'_i\theta'}}{\lambda'^2} = 6\nu\frac{G}{\lambda'^2}. \tag{27}$$

In other terms, the time scale τ' writes

$$\tau' = \frac{\lambda'^2}{6\nu}. \tag{28}$$

It is reasonable to assume that the two-point correlation between velocity and temperature in Eq. (24) can be linked to the two-point correlations $\overline{u'_\alpha(\mathbf{x})u'_\alpha(\mathbf{x}+r\,\mathbf{e}_\alpha)}$ and $\overline{\theta'(\mathbf{x})\theta'(\mathbf{x}+r\,\mathbf{e}_\alpha)}$. Introducing the Taylor micro-scales λ and λ_θ, respectively associated to these correlations, we assume the simple relation of proportionality

$$\lambda'^2 \propto \lambda\lambda_\theta \tag{29}$$

This particular relation is chosen among several possibilities because, as will be shown in Fig. 4, it leads to a dramatic improvement of the predictions in the natural convection regime. Since these Taylor micro-scales can be shown (e.g., Pope, 2000) to be directly related to dissipation rates as

$$\varepsilon \propto \nu\frac{u'^2}{\lambda^2} \text{ and } \varepsilon_\theta \propto \kappa\frac{\mathrm{k}_\theta}{\lambda_\theta^2}, \tag{30}$$

where $u' = (2k/3)^{1/2}$ and $k_\theta = \overline{\theta'^2}/2$, introducing Eq. (29) into Eq. (28) leads to

$$G_\varepsilon \propto \frac{\sqrt{Pr}\,G}{\sqrt{\tau\tau_\theta}} \tag{31}$$

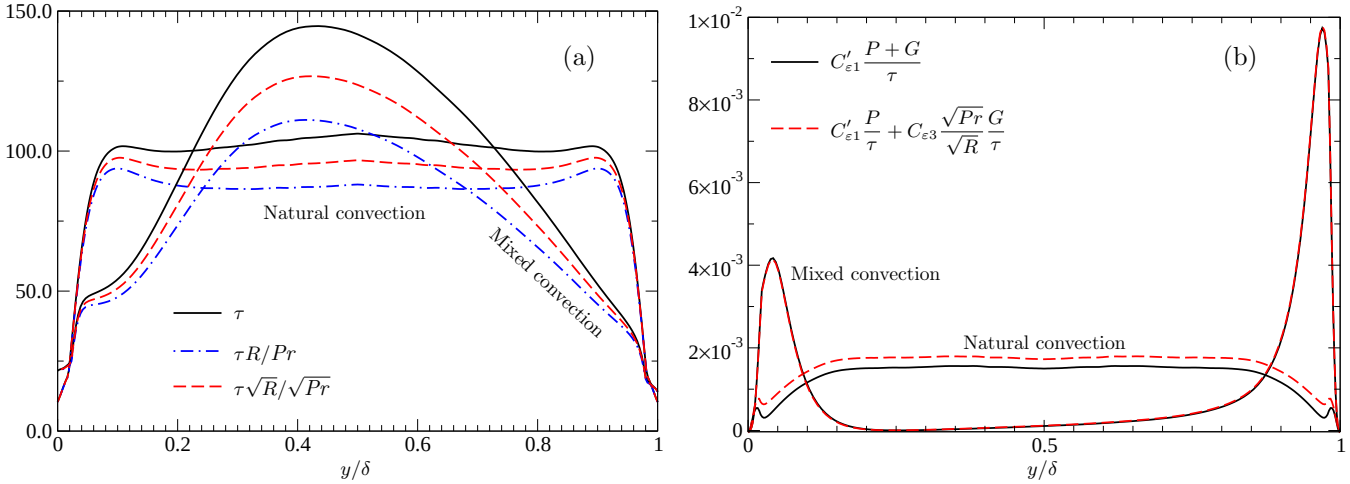

Figure 2: A priori tests in the case of the channel flow in mixed (Kasagi and Nishimura, 1997) and natural (Versteegh and Nieuwstadt, 1998) convection regimes. (a) Comparison of the mechanical, thermal and mixed time scales. (b) Comparison of the original and new models for the production terms in the dissipation equation. Data are in wall units.

where $\tau_\theta = \overline{\theta'^2}/\varepsilon_\theta$ is the thermal time scale. Introducing the thermal-to-mechanical time-scale ratio R, the production term in the ε-equation then reads

$$P_\varepsilon + G_\varepsilon = C'_{\varepsilon 1}\frac{P}{\tau} + C_{\varepsilon 3}\frac{\sqrt{Pr}}{\sqrt{R}}\frac{G}{\tau}, \tag{32}$$

i.e., the mixed time scale $\sqrt{R}\tau/\sqrt{Pr}$ substitutes for the mechanical time scale τ in the thermal part of production. Following Dehoux et al. (2012), we use a variable ratio R that goes to the correct limit $R = Pr$ at the wall and asymptotes to the constant value $R = R^h$ far from the wall:

$$R = R^h\alpha_\theta + (1-\alpha_\theta)Pr. \tag{33}$$

Note that, for the sake of consistency, the blending function in Eq. (33) is α_θ, in contrast to α_θ^3 in Dehoux et al. (2012).

It is noticeable that the square-root of the Prandtl number enters the mixed time scale in Eq. (32), as a consequence of the fact that G_ε is a term in the dissipation equation, i.e., is related to the dissipative scales. The appearance of the Prandtl number obviously comes from the contribution of the thermal field: if the Taylor micro-scale λ' was modelled as a pure thermal scale, i.e., $\lambda' = \lambda_\theta$, the time scale in Eq. (31) would be τ_θ/Pr. Since this dependence is supported by the analysis in homogeneous turbulence only, future work must be devoted to the investigation of the impact of this model on the prediction of buoyant flows of fluids with various Prandtl numbers in wall-bounded flows.

Fig. 2a shows a comparison of the mechanical, thermal and mixed time scales, using the DNS data for channel flows in the mixed (Kasagi and Nishimura, 1997) and natural convection regimes (Versteegh and Nieuwstadt, 1998). In both cases, the flow domain is bounded by two vertical, infinite parallel plates, separated by a distance $\delta = 2h$, with an imposed temperature difference Δ_θ. In the mixed convection case, a pressure gradient is imposed in order to generate an ascending flow: in the half-channel on the side of the hot wall (resp., cold wall), buoyancy tends to increase (resp., decrease) the flow rate and to reduce (resp., enhance) turbulence. The flow is characterized by three non-dimensional numbers: the friction Reynolds number $Re_\tau = 150$, the Grashof number $Gr = 9.6 \times 10^5$ and the Prandtl number $Pr = 0.71$. In the natural convection case, the vertical pressure gradient is zero, and the flow driven by buoyancy forces is characterized by the Prandtl number $Pr = 0.71$ and the Rayleigh number $Ra = 5 \times 10^6$.

It can be observed in Fig. 2a that the three time scales are equal in the vicinity of the wall, due to the fact that R asymptotically goes to Pr. In contrast, in the central region, the thermal time scale is significantly lower than the mechanical time scale, since $R/Pr \simeq 0.83$ and 0.77 for natural convection and mixed convection, respectively, such that the mixed time scale is about 0.91τ and 0.88τ, respectively.

For the natural convection case, the combination of the use of the mixed time scale in Eq. (32) and of a larger coefficient (the calibrated value of $C_{\varepsilon 3}$ is 2.02, while $C'_{\varepsilon 1}$ is between 1.4 and 1.5), leads to a significant increase of the production term in the dissipation equation, as shown in Fig. 2b: the production is 50% higher than with the original model in the region of the near-wall production peak, and 15% higher at the centreline. In contrast, for the mixed convection case, although the mixed time scale significantly differs from the mechanical time scale, the production rate in the dissipation equation is virtually unchanged (the difference is less than 1%), because the contribution of buoyancy production is small.

Moreover, time scales are also involved in the quasi-homogeneous and near-wall parts of the models for the $\phi_{i\theta}$ and $\varepsilon_{i\theta}$, in Eqs. (11), (12) and (13). For the sake of consistency, the same substitution is made in these models,

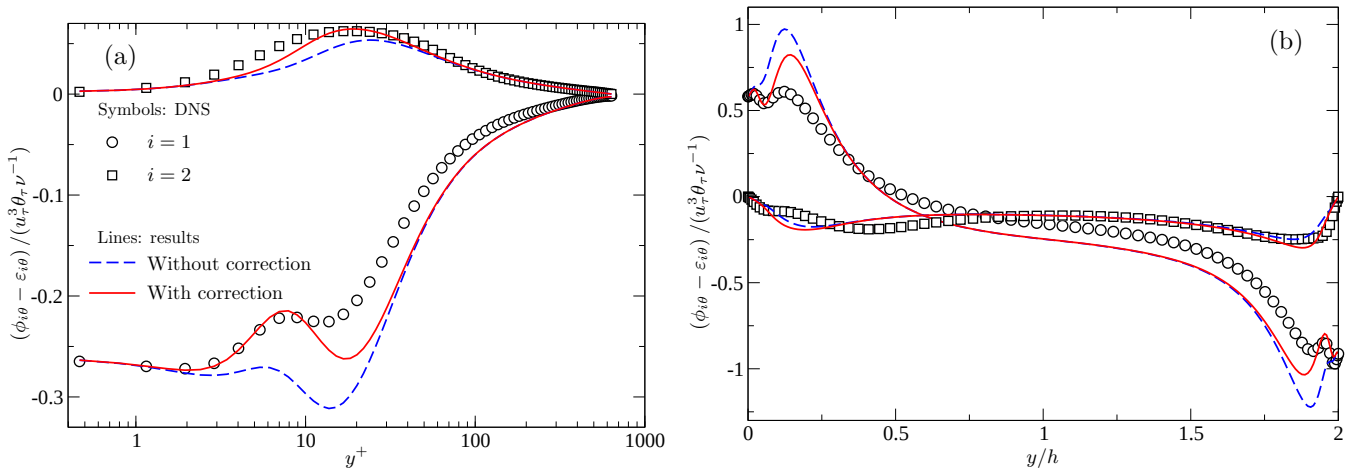

Figure 3: A priori test of the model for the difference $\phi_{i\theta} - \varepsilon_{i\theta}$ in turbulent channel flows. (a) Forced convection regime at $Re_\tau = 640$ and $Pr = 0.71$; DNS of Abe et al. (2004). (b) Mixed convection regime at $Re_\tau = 150$, $Pr = 0.71$ and $Ra = 6.82 \times 10^5$; DNS of Kasagi and Nishimura (1997) .

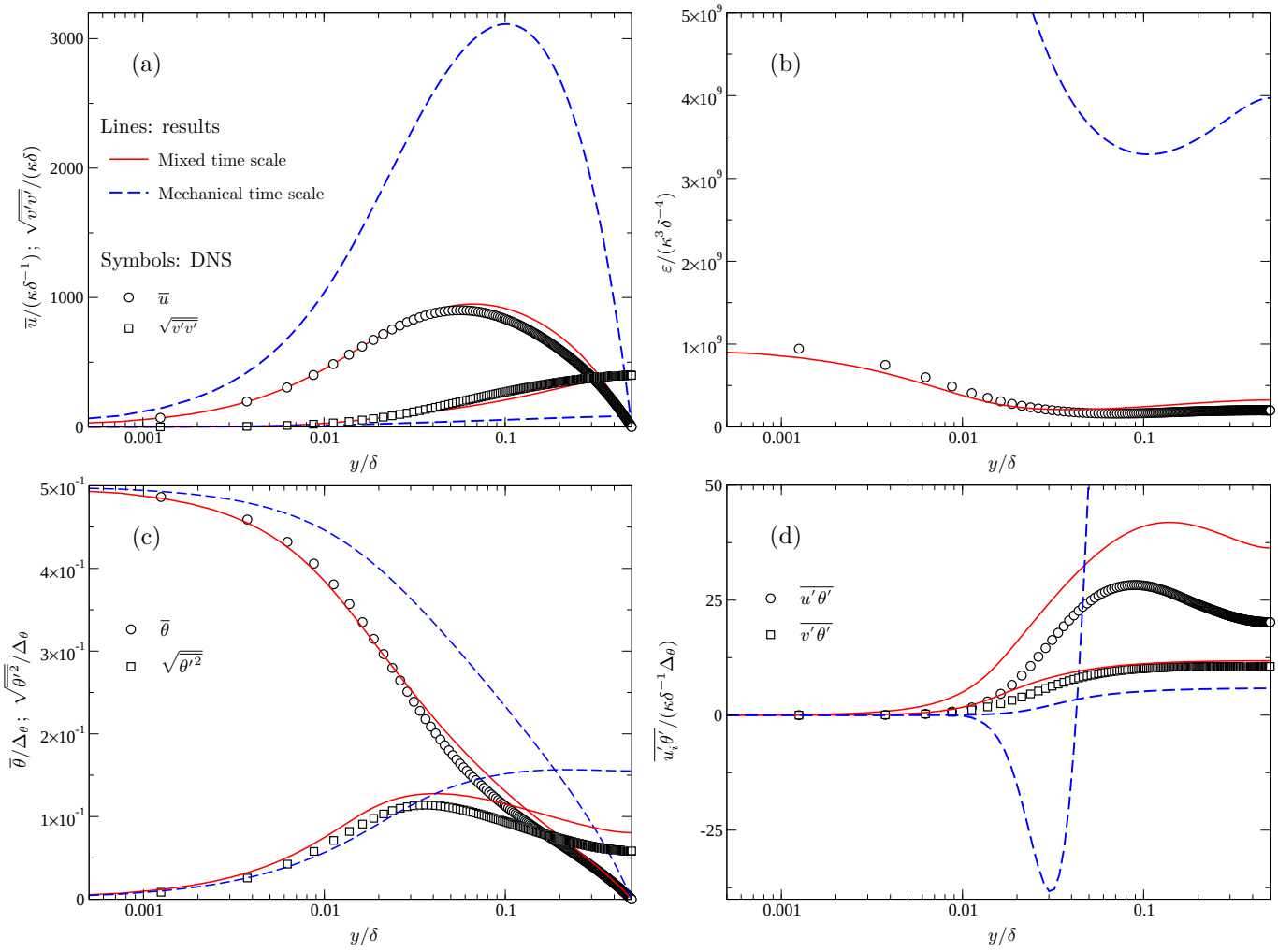

Figure 4: Turbulent channel in the natural convection regime at $Pr = 0.71$ and $Ra = 5 \times 10^6$. DNS data of Versteegh and Nieuwstadt (1998). Comparison of the results given by the EB-DFM using the mechanical time scale τ and the mixed time scale $\sqrt{R}\,\tau/\sqrt{Pr}$.

i.e., the mixed time scale $\sqrt{R}\,\tau/\sqrt{Pr}$ is used in lieu of τ. However, *a priori* tests shown in Fig. 3 for channel flows, in both the forced and mixed convection regimes, point out that these models require an additional modification. Indeed, it is observed, in both regimes, that the quasi-homogeneous model for the difference $\phi_{i\theta} - \varepsilon_{i\theta}$ rather satisfactorily reproduces this term in the central part of the channel, and that the near-wall model correctly provides the asymptotic behaviour in the very-near-wall region, but the predictions in the buffer layer are not fully satisfactory. The cause of this problem can be identified in Fig. 1: the buffer layer is not treated by a specific model, but rather by the blending of models dedicated to the near-wall and quasi-homogeneous regions, respectively. Therefore, specific modifications are introduced in the models given by Eqs. (12) and (13) for the near-wall terms $\phi^w_{i\theta}$ and $\varepsilon^w_{i\theta}$: similar to the case of the ε-equation, in which the ratio P/ε is used to promote production in the buffer layer (see Eq. 8), the models given by Eqs. (11), (12) and (13) (in which we use $\gamma_1 = 0$) are thus modified as

$$\phi^w_{i\theta} = -\frac{\sqrt{Pr}}{\sqrt{R}\tau}\left[1 + C^{\phi}_{w\theta}\,(1-\alpha_\theta)\,\frac{P+G}{\varepsilon}\right]\overline{u'_j\theta'}\,n_i n_j \tag{34}$$

$$\varepsilon^w_{i\theta} = \frac{\sqrt{Pr}}{\sqrt{R}\tau}C_\varepsilon\left[1 + C^{\varepsilon}_{w\theta}\,(1-\alpha_\theta)\,\frac{P+G}{\varepsilon}\right]\left(\overline{u'_i\theta'} + \overline{u'_j\theta'}\,n_i n_j\right) \tag{35}$$

As seen in Fig. 3, the factors in brackets are formulated in such a way that they do not affect the asymptotic behaviour, and help correcting the predictions in the buffer layer, and in particular significantly reduce the kinks observed in the buffer layer for the $i = 1$ component in both regimes.

In the natural convection regime, the time-scale modifications described above have a major impact on the predictions. This can be convincingly illustrated by comparing results obtained in the case of the differentially heated vertical channel flow presented above. The computations are carried out with EDF in-house open source (www.code-saturne.org) CFD software *Code_Saturne*. Details about the finite volume discretization scheme can be found in Archambeau et al. (2004).

Fig. 4 compares predictions for this case using either the mechanical or the modified time scale. It is observed that the results are drastically affected by this modification. It is well known that, in natural convection, since the flow is not driven by a pressure gradient, but rather by buoyancy, the coupling between the thermal and dynamic field is such that the flow is highly sensitive to modelling details. The use of an inaccurate model for the buoyancy production term G_ε in the dissipation equation leads to a severe overestimation of the dissipation rate, as seen in Fig. 4b, which strongly affects the other variables. The Reynolds stresses are much too weak, as illustrated by the profile of the wall-normal component $\overline{v'v'}$ in Fig. 4a, which yields a significant overestimation of the mean velocity. In Fig. 4c, it can be seen that the temperature profile is not correctly reproduced, due to the underestimation of the wall-normal heat flux $\overline{v'\theta'}$. The profiles of $\overline{u'\theta'}$ and $\sqrt{\overline{\theta'^2}}$ also illustrate the high sensitivity of this flow to an incorrect prediction of the dissipation rate.

These results highlight the importance of the choice of the time scale. Numerical experiments (not shown here) indicate that the influence of the mixed time scale in Eqs. (11), (12) and (13) is modest, albeit in the right direction: the keystone here is the time scale involved in the model given by Eq. (32) for the buoyancy production G_ε in the dissipation rate equation. Consequently, this mixed time scale will be used in the EB-RSM in the rest of the present paper, whatever the model used for the turbulent heat flux, ranging from GGDH to the full EB-DFM.

4. Validation

The present section aims at validating the turbulent heat flux model proposed in previous section by comparison with similar EB-DFM models already available in the literature (Shin et al., 2008; Choi and Kim, 2008) as well as simpler algebraic competitors, such as the generalized gradient diffusion hypothesis (GGDH, Daly and Harlow, 1970), the so-called algebraic flux model (AFM, Dol et al., 1997), and near-wall extensions using elliptic blending (EB-GGDH and EB-AFM, Dehoux et al., 2012). Comparisons are made with the standard DFM, which is not designed for near-wall regions, in order to quantify the improvement due to the introduction of near-wall effects. For a complete description of the models, see Appendix A and Appendix B. The test cases are selected in order to cover the full range of regimes, from forced to natural convection.

4.1. Channel flow in the forced convection regime

The channel flow in the forced convection regime of Abe et al. (2004) is first used for validation. The flow between two plates separated by δ is driven by a pressure gradient along the x-direction. A constant heat flux $\dot{q}_w$ and zero temperature fluctuations are imposed at the two walls, and temperature is considered a passive scalar. The flow is thus characterized by the two non-dimensional numbers $Re_\tau = 640$ and $Pr = 0.71$. The flow is periodic in the streamwise direction, and the friction Reynolds number Re_τ is imposed via a constant pressure gradient.

In this forced convection case, the dynamic field is not influenced by the choice of the heat flux model, such that the results are presented in Figs. 5a and b independently from the turbulent heat flux model. Consistent with Manceau (2015), it can be seen that the EB-RSM very accurately reproduces the mean velocity and Reynolds stresses in a channel flow. On the contrary, using the version used by Choi and Kim (2008), in which the coefficients have been modified in order to improve the predictions in natural convection flows, the results are not satisfactory. Two eddy-viscosity models (EVMs), widely used in the industry, the k–ω–SST model of Menter (1994) and the V2F

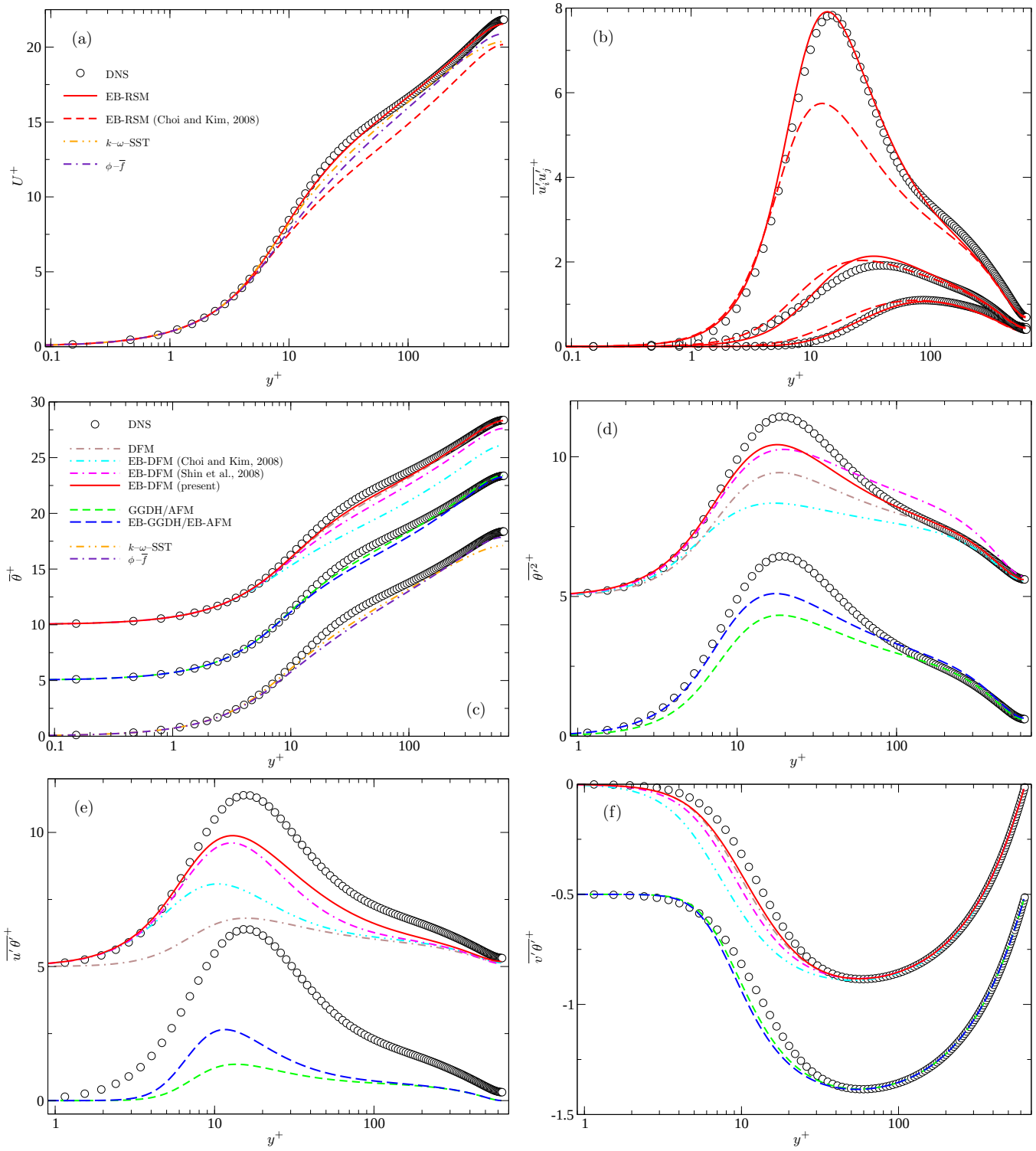

Figure 5: Channel flow in the forced convection regime of Abe et al. (2004) at $Re_\tau = 640$ and $Pr = 0.71$. (a) and (b) show the dynamic quantities given by the dynamic turbulence models. (c), (d), (e) and (f) show the thermal quantities given by the different models for the turbulent heat flux associated with the EB-RSM model and by the SGDH associated with the k–ω–SST and the ϕ–$\overline{f}$ models. For the sake of clarity, in (d), (e) and (f), results are shifted to form 2 categories: EB-RSM+differential flux models; EB-RSM+algebraic models; in (c), a third category is introduced: Eddy-viscosity models+SGDH.

model, using the stabilized formulation ϕ–$\overline{f}$ of Laurence et al. (2005), are also used for comparison. It is observed that the EB-RSM better reproduces the mean velocity profile than the two EVMs, in particular the ϕ–$\overline{f}$ model that underestimates the flow rate and overestimates the slope in the log layer.

Figs. 5c, 5d, 5e and 5f show the mean temperature, the temperature variance and two non-zero turbulent heat fluxes. In Figs. 5d, 5e and 5f, results are split into two groups, for the sake of clarity. The first group compares various differential flux models (DFMs) associated with the EB-RSM; the second group, algebraic models associated with the EB-RSM. All these models are detailed in Appendix B. A third group is included in Fig. 5c, which consists of the results of the simple gradient diffusion hypothesis (SGDH) associated to the EVMs, with $Pr_t = 1$.

Four DFMs are applied: the standard DFM (Launder, 1988), i.e., the model Eq. (11) used as the quasi-homogeneous part of our EB-DFM; the two EB-DFMs proposed by Choi and Kim (2008) and Shin et al. (2008), described in section 2; and, finally, the present modified formulation, described in section 3. It is seen in Figs. 5c–f that, in association with the EB-RSM that correctly reproduces the anisotropy of the Reynolds stress, the standard DFM, which does not contain any explicit accounting of wall blockage, is nonetheless able to very well reproduce the wall-normal heat flux $\overline{v'\theta'}$ and, consequently, the mean temperature profile. The wall-parallel flux $\overline{u'\theta'}$ is severely underestimated, which can be detrimental in more complex configurations, but obviously does not have any effect in the present case. This component, as well as the temperature variance, are significantly improved by the introduction of elliptic blending (EB) in the DFM, similar to what was observed by Dehoux et al. (2012) with algebraic models. It is worth emphasizing that, although $\overline{\theta'^2}$ has no effect on the velocity and temperature fields in the forced convection regime, it might be crucial for the prediction of thermal fatigue in conjugate heat transfer problems (Howard and Serre, 2015). However, the EB-DFM of Choi and Kim (2008), calibrated for natural convection, is not satisfactory in the forced convection regime, which is mainly due to the inaccurate reproduction of the dynamic field, as a consequence of the modification of the coefficients of the EB-RSM. For this reason, this model is abandoned in the rest of the present article. Finally, it is seen that the present modifications to the EB-DFM improve the predictions of all the variables compared to the EB-DFM of Shin et al. (2008).

Two algebraic models are also associated with the EB-RSM: the GGDH, and the EB-GGDH proposed by Dehoux et al. (2012), which is an algebraic truncation of the EB-DFM. Note that in this forced convection test case, the AFM and the GGDH yields identical results. This remark holds for the EB-AFM and EB-GGDH as well. It can be observed in Fig. 5c that, when associated to the EB-RSM, the GGDH yields satisfactory predictions in this forced convection case. The main limitation is again the underestimation of $\overline{u'\theta'}$, which is, as said above, not active in the present flow. This heat flux and the temperature variance are, as was observed for the DFMs, improved by the introduction of elliptic blending, but the prediction of $\overline{v'\theta'}$ and, consequently, of the mean temperature, are slightly degraded. The reasons for the relative success of the GGDH, despite the lack of wall-blockage modelling, is however a coincidence, as explained in Dehoux et al. (2012).

Finally, the two EVMs, associated with the SGDH, honourably reproduce the mean temperature profile, since, in this forced convection case, the constant turbulent Prandtl number hypothesis is sufficient to correctly reproduce the turbulent diffusion, as soon as the eddy-viscosity ν_t is correctly damped in the near-wall region, which is the case with the k–ω–SST and ϕ–$\overline{f}$ models.

4.2. Channel flow in the mixed convection regime

The second test case selected for validation is the channel flow in the mixed convection regime (Kasagi and Nishimura, 1997) at $Re_\tau = 150$, $Gr = 9.6\times10^5$ and $Pr = 0.71$, described in section 3.2. Fig. 6 shows the results obtained for this configuration using, as in Fig. 5 for the forced convection regime, different combinations of dynamic and thermal models. It can be seen in Figs. 6a and b that the dynamic field is only marginally influenced by the turbulent heat flux model. The EB-RSM reproduces the mean velocity and turbulent energy profiles more accurately than the EVMs. In particular, the k–ω–SST model significantly underestimates the peaks of k in the near-wall regions.

Fig. 6c shows that, apart from the ϕ–$\overline{f}$ model, which severely overestimates the temperature in the central part of the channel, all the models fairly well reproduce the mean temperature profile. The DFM and EB-DFM predictions are superimposed. The impact of the introduction of the wall blockage modelling (EB) is visible in Fig. 6d for the temperature variance, and, above all, in Fig. 6e, where the improvement of the prediction of the wall-parallel heat flux $\overline{u'\theta'}$ is very significant. With the exception of the temperature variance, the EB-DFM of Shin et al. (2008) yields less accurate results, due to an underestimation of the wall-normal flux $\overline{v'\theta'}$ in a small region around $y/h = 0.3$.

Algebraic models yield very satisfactory results in general, when associated with the EB-RSM. The results for the GGDH and AFM models, in both their standard and EB versions, are superimposed in Figs. 6c, d and f, since they are only distinguished by the buoyant term $-\beta g\overline{\theta'^2}$ in the algebraic relation for $\overline{u'\theta'}$. In Fig. 6e, it can be observed that the AFM is superior to the GGDH, and that the introduction of wall blockage is very favourable.

The EB-DFM and EB-AFM lead to very similar results, which suggests that the assumptions made by Dehoux et al. (2012) to derive the algebraic version of the EB-DFM are valid in this case. However, it is observed in Fig. 6e that spatial variations of the wall-parallel heat flux

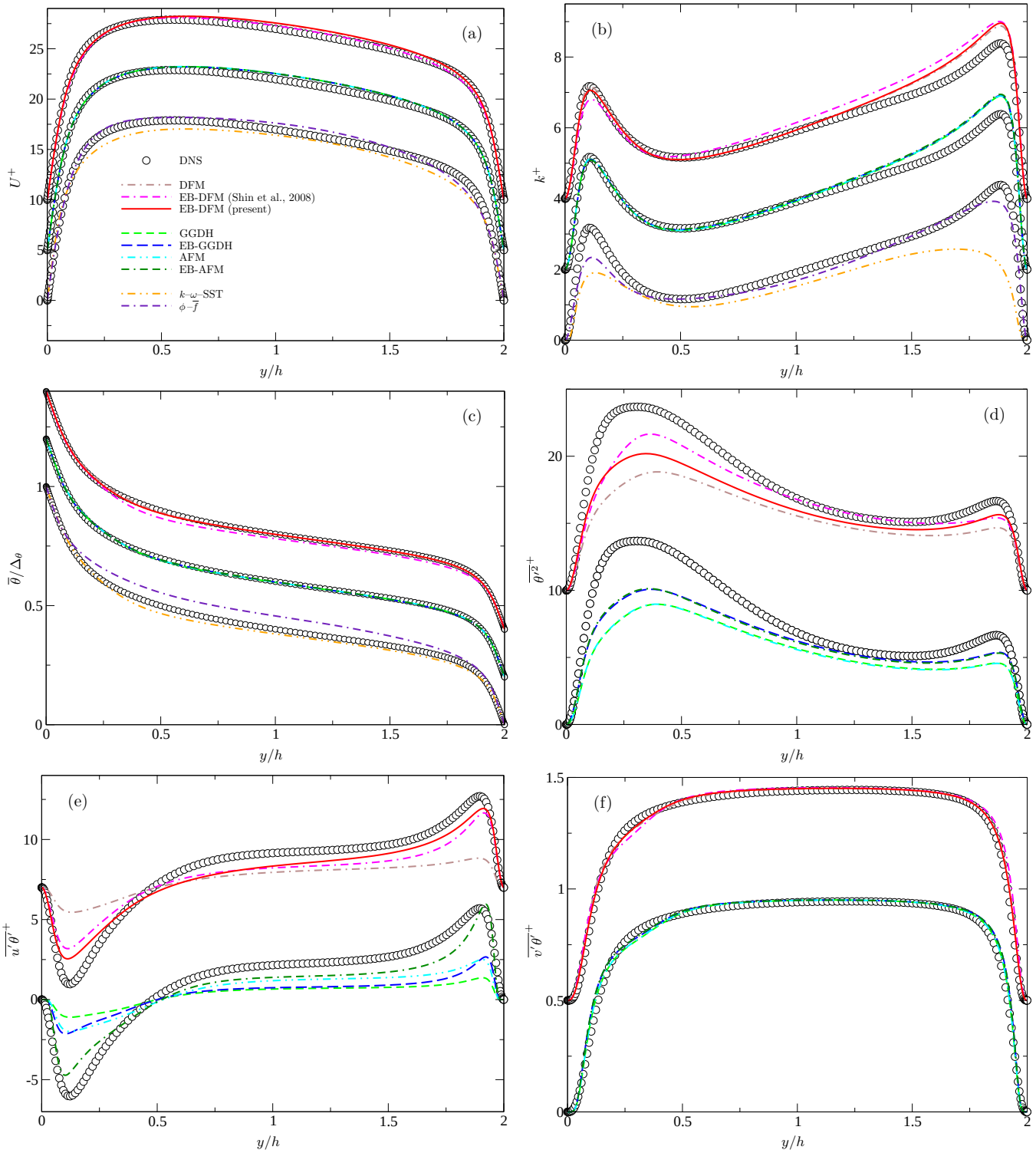

Figure 6: Profiles similar to those of Fig. 5, but for the case of the channel flow in the mixed convection regime of Kasagi and Nishimura (1997) at $Re_\tau = 150$, $Gr = 9.6 \times 10^5$ and $Pr = 0.71$.

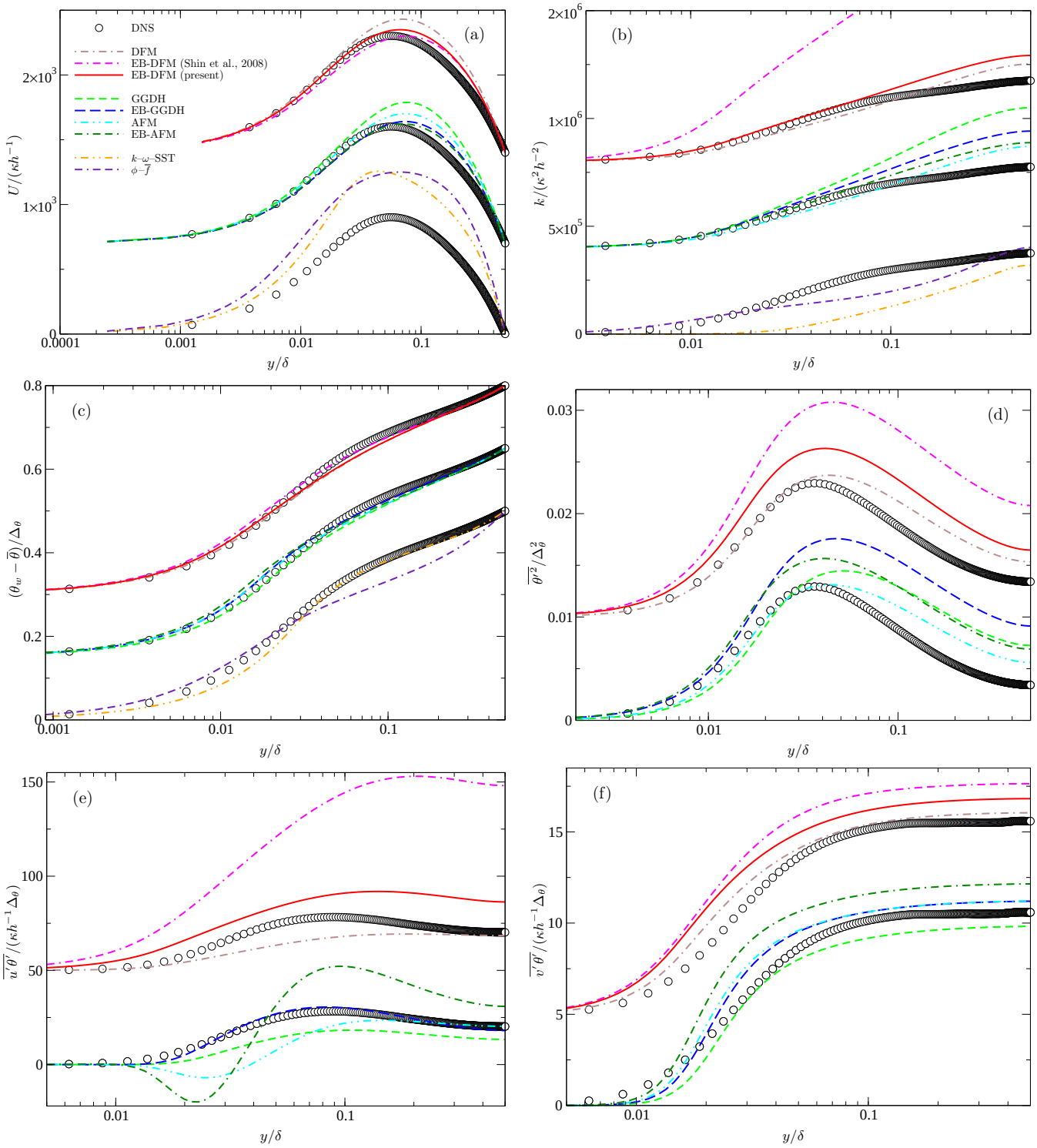

Figure 7: Profiles similar to those of Fig. 5, but for the case of the channel flow in natural convection regime of Versteegh and Nieuwstadt (1998) at $Pr = 0.71$ and $Ra = 5 \times 10^6$.

$\overline{u'\theta'}$ are steeper with the EB-AFM than with the EB-DFM, due to the assumptions made about diffusion.

4.3. Channel flow in natural convection regime

The natural convection test case of Versteegh and Nieuwstadt (1998) has already been introduced in section 3.2 in order to illustrate the influence of the time scale. Since the flow is uniquely driven by buoyancy, the turbulent heat flux model now plays a major role in the predictions of both the dynamic and thermal fields. It is recalled that the mixed time scale proposed in section 3.2 is used in all the EB-RSM computations, whether it is associated with the DFM, the EB-DFM, the GGDH, the EB-GGDH, the AFM or the EB-AFM. The comparison with the EB-DFM of Shin et al. (2008) illustrates the influence of all the modifications proposed in section 3. Many additional tests (not shown here, for the sake of concision) have been performed to investigate the individual influence of each modification (Dehoux, 2012).

Fig. 7 shows that both the DFM and EB-DFM globally lead to very satisfactory predictions. The introduction of elliptic blending is not decisive here: the turbulent quantities are as well reproduced with the DFM than with the EB-DFM, if not slightly better. The temperature profiles are superimposed, and only the mean velocity prediction is slightly improved with the EB-DFM. The model of Shin et al. (2008) reproduces fairly well the mean velocity and temperature profiles, despite a severe overestimation of the turbulent quantities, as seen in Figs. 7b, d, e and f. The use of a mechanical time scale in this model is very detrimental, and the authors have compensated this problem by increasing the coefficient g_6 in ϕ^h_{ij} (Eq. 2). Indeed, the influence of buoyancy in the redistribution term is modelled as an isotropization of production

$$-g_6\left(G_{ij}-\frac{2}{3}G\delta_{ij}\right). \tag{36}$$

Shin et al. (2008) have increased the coefficient g_6 from the standard value 0.5 to 1.5, in order to improve the predictions in natural convection flows. However, it must be emphasized that this coefficient should be less than unity, otherwise unphysical results can be observed. For instance, the contribution of buoyancy to the production and redistribution terms in the $\overline{u'v'}$-equation in the present configuration is, far from the wall ($\alpha = 1$),

$$G_{12} - g_6\, G_{12} = -(1-g_6)\beta g\overline{v'\theta'}. \tag{37}$$

If $g_6 < 1$, the sum of the two terms is of the same sign as the buoyancy production term G_{12} alone, such that the redistribution term only weakens the generation of anisotropy by G_{12}, hence the name *isotropization of production*. If $g_6 > 1$, the sign of the sum is changed, which does not conform to the generally admitted interpretation of the role of the redistribution term.

Algebraic models give good results in this natural convection case. The use of a mixed time scale in the ε-equation is crucial here: indeed, this test case was not used in Dehoux et al. (2012) since it was not possible to obtain satisfactory results. Moreover, the same conclusion can be drawn as for the EB-DFM: the modelling of the effects of wall blockage on the heat fluxes does not appear crucial; only the prediction of the mean velocity profile is slightly improved by the EB-GGDH and EB-AFM, as compared to the GGDH and AFM, respectively. The main drawback of the AFM and EB-AFM compared to their parent DFMs is the appearance of negative excursions of the wall-parallel component $\overline{u'\theta'}$ of the turbulent heat flux in the near-wall region, which is a consequence of the simplifying hypotheses about diffusion made during the derivation of the algebraic models from the DFMs (Dehoux et al., 2012). The even simpler gradient models GGDH and EB-GGDH do not exhibit the same problem, and globally give surprisingly good results in the present case. However, as mentioned for instance by Hanjalić (2002), it is desirable to retain all the production mechanisms in the heat flux model, since in some cases, such as Rayleigh-Bénard convection, the only non-zero source of turbulent mixing of heat is buoyancy production $-\beta g_i\overline{\theta'^2}$.

Finally, the two eddy-viscosity models do not show results as accurate as the EB-RSM associated to the various heat flux models, but at varying degrees. The ϕ–$\overline{f}$ model does not correctly reproduce the mean temperature profile, and severely overestimates the mean velocity. The k–ω–SST yields a similar prediction of the mean velocity, although the turbulent energy is strongly underestimated, and fairly well reproduces the mean temperature profile.

4.4. Trias et al.'s cavity

The case of a differentially heated cavity, computed in DNS by Trias et al. (2007), is described in Fig. 8. The height-to-width aspect ratio of the cavity is equal to 4. The domain is infinite (periodic) in the z-direction. The motion is generated by the temperature difference between the two lateral walls, such that it is characterized by two non-dimensional numbers: the Rayleigh number $Ra = 10^{11}$ (based on the cavity height) and the Prandtl number $Pr = 0.71$. In this configuration, the flow is laminar or almost laminar in a large portion of the domain along the vertical walls and transitions to turbulence in the upper part of the boundary layer along the hot wall, and in the lower part along the cold wall. Due to the central symmetry, it is sufficient to plot the results along the hot wall.

Three models, representative of the three groups used in previous section, relatively successful in channel flows in the three convection regimes, are applied to the present case: the EB-DFM and the AFM, both associated to the EB-RSM, and the k–ω–SST model, which is widely used in the energy production industry.

Figs. 9, 10 and 11 show profiles extracted along the horizontal, x-axis, at several heights in the cavity. DNS data show that transition occurs at about $y/H = 0.40$, but the velocity profile remains basically unchanged until $y/H = 0.6$, where turbulent diffusion starts to enlarge and reduce the velocity peak. It is observed that the prediction

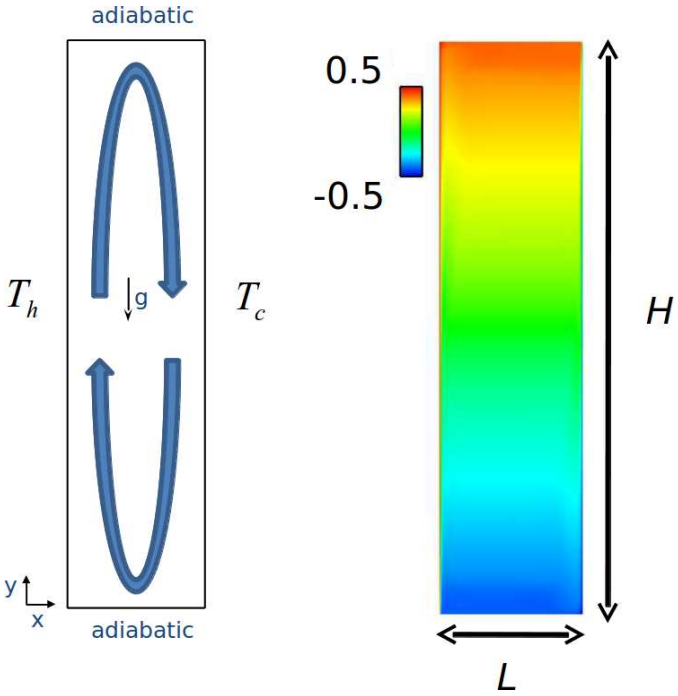

Figure 8: (left) Configuration of the test case of Trias et al. (2007); (right) temperature field in the cavity (the origin of the coordinate frame is at the bottom left corner).

of transition is strongly dependent on the model. It can be seen, for instance on k or $\overline{\theta'^2}$ profiles (Figs. 9 and 10, respectively), that the eddy-viscosity model yields much too early a transition to turbulence, whereas the EB-RSM, combined with EB-DFM or AFM, gives a slightly too late transition.

In Fig. 9, it is observed that the vertical mean velocity $\overline{v}$ is much better predicted by the EB-RSM, associated with either the EB-DFM or the AFM, than with the eddy-viscosity model. The k–ω–SST yields discrepant profiles in particular in the region between $y/H = 0.3$ and $y/H = 0.6$, which is clearly due to the early transition to turbulence that leads to a severe overestimation of turbulent diffusion. The AFM transitions slightly earlier than the EB-DFM, as can be seen at $y/H = 0.5$ in Fig. 9(left), such that the mean velocity profile is slightly better predicted at $y/H = 0.6$ by the AFM. These two models are able to correctly reproduce the turbulent energy for $y/H \geq 0.9$, where turbulence is developed, but the double peak observed close to the wall in the transitional region is missed.

Fig. 10 shows the mean temperature and the temperature variance profiles. Although they predict a slightly too late transition, the EB-DFM and the AFM both very well predict the mean temperature. Indeed, as mentioned above about the velocity profile, turbulence starts smoothing the quasi-laminar profiles above $y/H = 0.6$ only, such that the underestimation of the wall-normal heat flux $\overline{u'\theta'}$ for $y/H \leq 0.6$, seen in Fig. 11, does not affect the mean temperature profile. On the contrary, the early transition given by the k–ω–SST, which leads to a strong overestimation of $\overline{u'\theta'}$ up to $y/H = 0.5$, is detrimental to the reproduction of the mean temperature profile.

In Fig. 11(right), it is seen that the three models are unable to correctly reproduce the wall-parallel component $\overline{v'\theta'}$. By definition, the SGDH relates this component to the vertical gradient of the mean temperature, which is close to zero. The other two models are able to correctly predict the profile of $\overline{v'\theta'}$ in the region $y/H \geq 0.9$, but the complex shape of the profile, linked to the complex shape of the turbulent energy observed in Fig. 9(right), is not reproduced.

In general, it can be seen that the EB-RSM, associated with either the EB-DFM or the AFM, yield satisfactory predictions of the mean velocity and temperature profiles, although the delay in the transition to turbulence along the wall is detrimental to the accuracy of the results. In contrast, the k–ω–SST model associated with the SGDH exhibits much too early a transition, which leads to inaccurate mean dynamics and thermal fields.

5. Conclusion

The elliptic blending (EB) strategy, proposed by Manceau and Hanjalić (2002) for representing the effects of wall blockage on the Reynolds stresses, can be extended to the modelling of the turbulent heat fluxes, in the framework of differential flux models (DFMs), leading to the EB-DFM. In the present work, modifications of the EB-DFMs proposed by Shin et al. (2008) and Choi and Kim (2008) are introduced in order to improve the predictions of the dynamic and thermal fields in forced, mixed and natural convection regimes. It can be shown, following the proposal of Dehoux et al. (2012) in the framework of algebraic heat flux models, that the length scale driving the thermal elliptic blending parameter must be different from the length scale of the mechanical elliptic blending parameter. But the most important modification is the substitution of a mixed time scale for the mechanical time scale in the buoyancy production term of the dissipation equation, which has a drastic impact on the predictions in the natural convection regime.

The relevance of these modifications is demonstrated by *a priori* tests and computations in the different convection regimes, in comparison with the models of Shin et al. (2008) and Choi and Kim (2008). Moreover, linear eddy-viscosity models, such as the V2F model (here the robust formulation ϕ–$\overline{f}$), and the k–ω–SST model that is widely used in the industry of energy production, yield satisfactory results for forced convection, but their predictions deteriorate with the increasing influence of buoyancy. In contrast, algebraic models, either the generalized gradient diffusion hypothesis (GGDH) or the so-called algebraic flux model (AFM), with or without elliptic blending, are able to fairly well reproduce the three convection regimes, as soon as they are associated with the version of the EB-RSM using the mixed time scale in the turbulent dissipation equation.

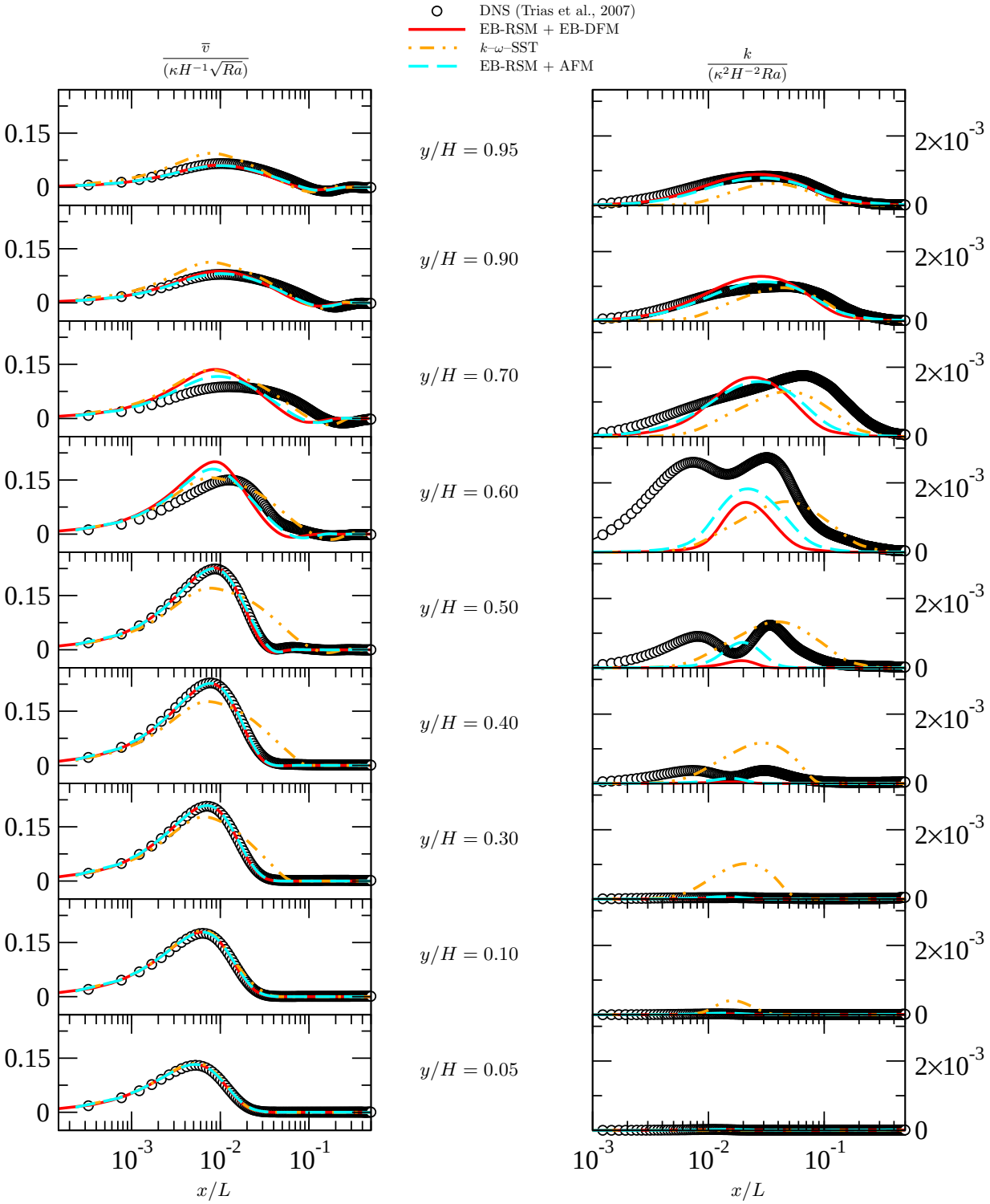

Figure 9: Differentially heated cavity flow of Trias et al. (2007) with aspect ratio 4, $Pr = 0.71$ and $Ra = 10^{11}$. Vertical component of the mean velocity (left) and turbulent energy (right). Profiles are extracted along the wall-normal direction, on the side of the hot wall, at 9 different heights.

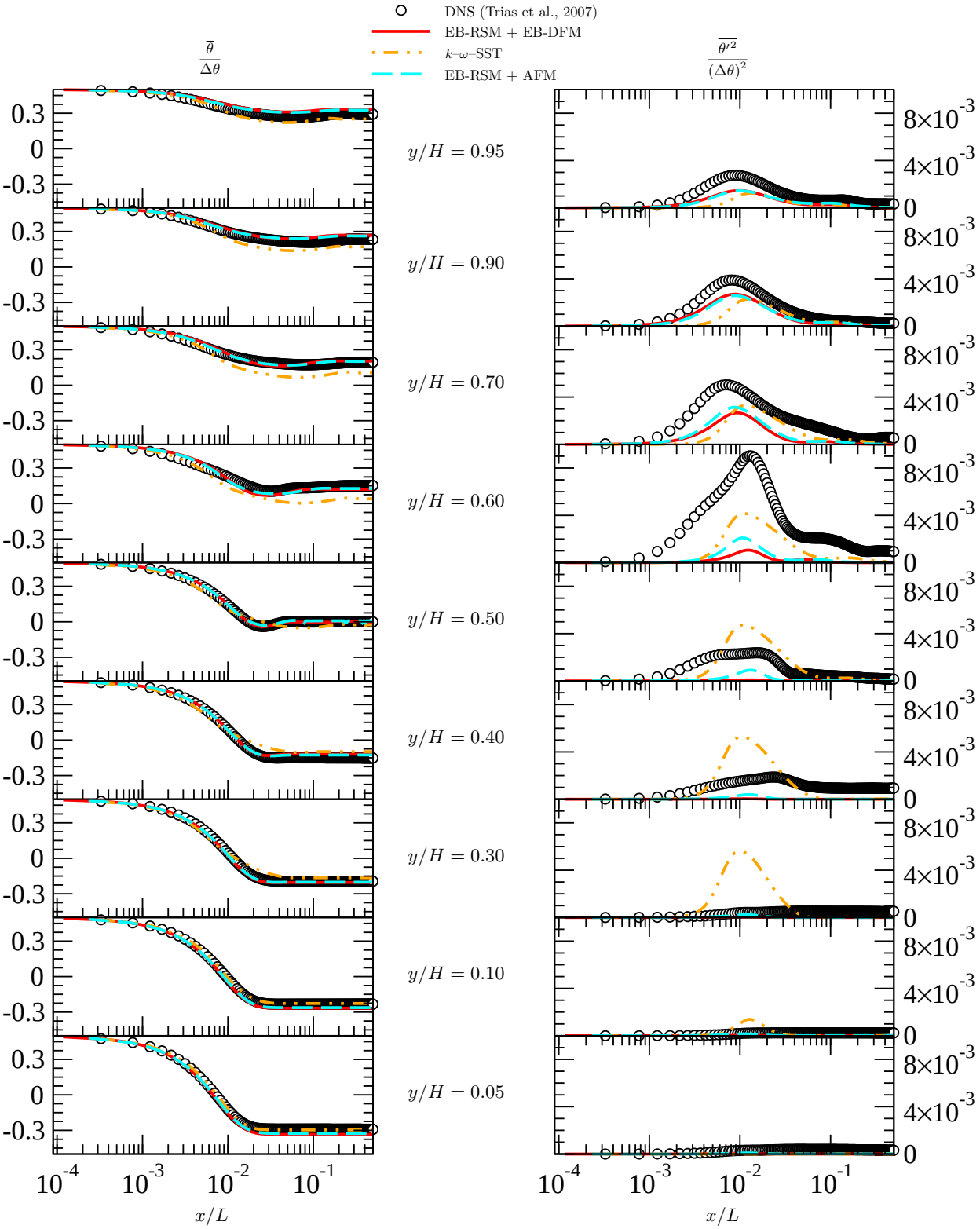

Figure 10: Profiles similar to those of Fig. 9, but for the mean temperature (left) and the temperature variance (right).

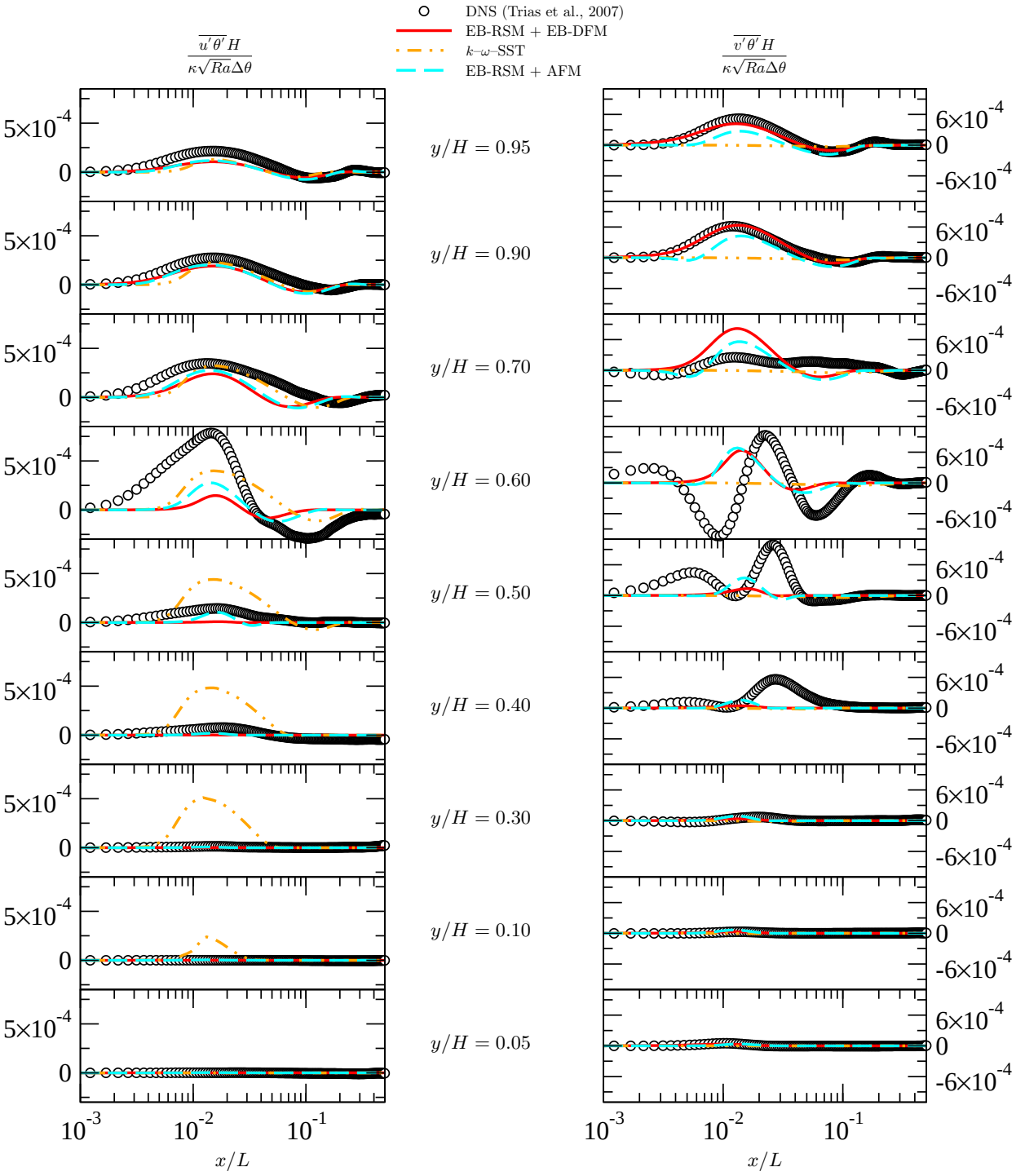

Figure 11: Profiles similar to those of Fig. 9, but for the wall-normal turbulent heat flux $\overline{u'\theta'}$ (left) and the wall-parallel turbulent heat flux $\overline{v'\theta'}$ (right)

These results, although they are limited to academic channel flow and 2D cavity configurations, are very promising, and it is worth pointing out that sophisticate models, even the EB-DFM associated with EB-RSM, were found numerically stable, which is crucial for future industrial applications.

Acknowledgements

The authors acknowledge the ANRT for its contribution in funding the present study (CIFRE 2009/0079).

Appendix A. Model for the dynamic field (EB-RSM)

$$\begin{aligned}\frac{\mathrm{D}\overline{u_i'u_j'}}{\mathrm{D}t} &= -\overline{u_i'u_k'}\frac{\partial\overline{u_j}}{\partial x_k} - \overline{u_j'u_k'}\frac{\partial\overline{u_i}}{\partial x_k} - g_i\beta\overline{u_j'\theta'} - g_j\beta\overline{u_i'\theta'} + \phi_{ij}^* \\ &\quad -\varepsilon_{ij} + \frac{\partial}{\partial x_k}\left(\nu\frac{\partial\overline{u_i}}{\partial x_k}\right) + \frac{\partial}{\partial x_l}\left(\frac{C_\mu}{\sigma_k}\overline{u_l'u_m'}\,\tau\frac{\partial\overline{u_i'u_j'}}{\partial x_m}\right)\end{aligned} \tag{A.1}$$

$$\varepsilon_{ij} = (1-\alpha^3)\frac{\overline{u_i'u_j'}}{k}\varepsilon + \frac{2}{3}\alpha^3\varepsilon\delta_{ij} \tag{A.2}$$

$$\phi_{ij}^* = (1-\alpha^3)\phi_{ij}^w + \alpha^3\phi_{ij}^h \tag{A.3}$$

$$\begin{aligned}\phi_{ij}^w &= -5\frac{\varepsilon}{k}\Bigg[\overline{u_iu_k}n_jn_k + \overline{u_ju_k}n_in_k \\ &\quad -\frac{1}{2}\overline{u_ku_l}n_kn_l\left(n_in_j+\delta_{ij}\right)\Bigg]\end{aligned} \tag{A.4}$$

$$\mathbf{n} = \frac{\boldsymbol{\nabla}\alpha}{\|\boldsymbol{\nabla}\alpha\|} \tag{A.5}$$

$$\begin{aligned}\phi_{ij}^h &= -\left(g_1+g_1^*\frac{P}{\varepsilon}\right)\varepsilon b_{ij} + \left(g_3 - g_3^*\sqrt{b_{kl}b_{kl}}\right)kS_{ij} \\ &\quad +g_4k\left(b_{ik}S_{jk}+b_{jk}S_{ik}-\frac{2}{3}b_{lm}S_{lm}\delta_{ij}\right) \\ &\quad +g_5k\left(b_{ik}W_{jk}+b_{jk}W_{ik}\right) - g_6\left(G_{ij}-\frac{2}{3}G\delta_{ij}\right)\end{aligned} \tag{A.6}$$

$$g_1 = 3.4;\ g_1^* = 1.8;\ g_3 = 0.8;\ g_3^* = 1.3;$$

$$g_4 = 1.25;\ g_5 = 0.4;\ g_6 = 0.5 \tag{A.7}$$

$$b_{ij} = \frac{\overline{u_i'u_j'}}{2k} - \frac{1}{3}\delta_{ij} \tag{A.8}$$

$$S_{ij} = \frac{1}{2}\left(\frac{\partial U_i}{\partial x_j}+\frac{\partial U_j}{\partial x_i}\right)\ ;\quad W_{ij} = \frac{1}{2}\left(\frac{\partial U_i}{\partial x_j}-\frac{\partial U_j}{\partial x_i}\right) \tag{A.9}$$

$$\alpha - L^2\nabla^2\alpha = 1 \tag{A.10}$$

$$L = C_L\max\left(\frac{k^{3/2}}{\varepsilon}, C_\eta\frac{\nu^{3/4}}{\varepsilon^{1/4}}\right) \tag{A.11}$$

$$\begin{aligned}\frac{\mathrm{D}\varepsilon}{\mathrm{D}t} &= C_{\varepsilon1}'\frac{P}{\tau} - C_{\varepsilon_2}\frac{\varepsilon}{\tau} + C_{\varepsilon3}\frac{\sqrt{Pr}}{\sqrt{R}}\frac{G}{\tau} \\ &\quad +\frac{\partial}{\partial x_l}\left(\frac{C_\mu}{\sigma_\varepsilon}\overline{u_lu_m}\,\tau\frac{\partial\varepsilon}{\partial x_m}\right) + \nu\frac{\partial^2\varepsilon}{\partial x_k\partial x_k}\end{aligned} \tag{A.12}$$

$$\tau = \max\left(\frac{k}{\varepsilon}, C_T\left(\frac{\nu}{\varepsilon}\right)^{1/2}\right) \tag{A.13}$$

$$C_{\varepsilon_1}' = C_{\varepsilon_1}\left[1 + A_1\left(1-\alpha^3\right)\frac{P}{\varepsilon}\right] \tag{A.14}$$

$$C_\mu = 0.21;\ \sigma_k = 1.0;\ C_T = 6.0; C_L = 0.125;$$

$$C_\eta = 80.0;\ C_{\varepsilon_1} = 1.44;\ C_{\varepsilon_2} = 1.83;$$

$$C_{\varepsilon_3} = 2.02;\ A_1 = 0.1;\ \sigma_\varepsilon = 1.15 \tag{A.15}$$

Appendix B. Models for the thermal field

Appendix B.1. EB-DFM

$$\begin{aligned}\frac{\mathrm{D}\overline{u_i'\theta'}}{\mathrm{D}t} &= -\overline{u_k'\theta'}\frac{\partial\overline{u_i}}{\partial x_k} - \overline{u_i'u_k'}\frac{\partial\overline{\theta}}{\partial x_k} - \beta g_i\overline{\theta'^2} \\ &\quad +\phi_{i\theta}^* - \varepsilon_{i\theta} + \frac{\partial}{\partial x_k}\left(C_\theta\overline{u_k'u_l'}\tau\frac{\partial\overline{u_i'\theta'}}{\partial x_l}\right) \\ &\quad +\frac{\partial}{\partial x_k}\left(\frac{\kappa+\nu}{2}\frac{\partial\overline{u_i'\theta'}}{\partial x_k} + \gamma_2n_in_j\frac{\nu-\kappa}{6}\frac{\partial\overline{u_j'\theta'}}{\partial x_k}\right)\end{aligned} \tag{B.1}$$

$$\varepsilon_{i\theta} = \left(1-\alpha_\theta\right)\varepsilon_{i\theta}^w + \alpha_\theta\varepsilon_{i\theta}^h \tag{B.2}$$

$$\varepsilon_{i\theta}^w = \frac{\sqrt{Pr}}{\sqrt{R}T}C_\varepsilon\left[1 + C_{w\theta}^\varepsilon\left(1-\alpha_\theta\right)\frac{P+G}{\varepsilon}\right]\left(\overline{u_i'\theta'} + \overline{u_j'\theta'}n_in_j\right) \tag{B.3}$$

$$\varepsilon_{i\theta}^h = 0 \tag{B.4}$$

$$\phi_{i\theta}^* = \left(1-\alpha_\theta\right)\phi_{i\theta}^w + \alpha_\theta\phi_{i\theta}^h \tag{B.5}$$

$$\phi_{i\theta}^h = -\frac{\sqrt{R^h}}{\sqrt{R}T}C_{1\theta}\overline{u_i'\theta'} + C_{2\theta}\overline{u_j'\theta'}\frac{\partial\overline{u_i}}{\partial x_j} + C_{3\theta}\beta g_i\overline{\theta'^2} \tag{B.6}$$

$$\phi_{i\theta}^w = -\frac{\sqrt{Pr}}{\sqrt{R}T}\left[1 + C_{w\theta}^\phi\left(1-\alpha_\theta\right)\frac{P+G}{\varepsilon}\right]\overline{u_j'\theta'}n_in_j \tag{B.7}$$

$$C_\theta = 0.22;\ C_{w\theta}^\phi = 2;\ C_{w\theta}^\varepsilon = -0.3 \tag{B.8}$$

$$\alpha_\theta - L_\theta^2\nabla^2\alpha_\theta = 1 \tag{B.9}$$

$$L_\theta = 2.5L \tag{B.10}$$

$$T = \frac{k}{\varepsilon};\; C_\varepsilon = \frac{1}{2}\left(1 + \frac{1}{Pr}\right);\; C_{1\theta} = 4.15;$$

$$C_{2\theta} = 0.3;\; C_{3\theta} = 0.5 \tag{B.11}$$

$$\begin{aligned}\frac{\mathrm{D}\overline{\theta'^2}}{\mathrm{D}t} &= -2\overline{u_k'\theta'}\frac{\partial\overline{\theta}}{\partial x_k} - \frac{\overline{\theta'^2}}{R}\frac{\varepsilon}{k} + \frac{\partial}{\partial x_k}\left(\frac{\nu}{Pr}\frac{\partial\overline{\theta'^2}}{\partial x_k}\right) \\ &\quad + \frac{\partial}{\partial x_k}\left(C_{\theta\theta}\,\overline{u_k'u_l'}\tau\frac{\partial\overline{\theta'^2}}{\partial x_l}\right)\end{aligned} \tag{B.12}$$

$$R = (1-\alpha_\theta)\,Pr + \alpha_\theta R^h \tag{B.13}$$

$$R^h = 0.5;\; C_{\theta\theta} = 0.21 \tag{B.14}$$

Appendix B.2. DFM

The DFM is obtained by applying $\alpha_\theta = 1$ in the equations of Appendix B.1.

Appendix B.3. EB-AFM

The EB-AFM makes use of Eqs. (B.9) to (B.14) and

$$\begin{aligned}\overline{u_i'\theta'} &= -C_\theta T\left[\overline{u_i'u_j'}\frac{\partial\overline{\theta}}{\partial x_j} + \xi\overline{u_j'\theta'}\frac{\partial\overline{u_i}}{\partial x_j} + \eta\beta g_i\overline{\theta'^2}\right. \\ &\quad \left. + \chi\frac{\varepsilon}{k}\overline{u_j'\theta'}n_in_j\right]\end{aligned} \tag{B.15}$$

$$C_\theta = \frac{\sqrt{R}C_\theta'}{\alpha_\theta C_{1\theta}\sqrt{R^h} + (1-\alpha_\theta)\sqrt{Pr}\left[C_\varepsilon\left(1 + C_\theta'\sqrt{R}\right) + C_\theta'\sqrt{R}\right]} \tag{B.16}$$

$$C_\theta' = 0.91;\; \xi = (1 - \alpha_\theta C_{2\theta});$$

$$\eta = (1 - \alpha_\theta C_{3\theta});\; \chi = (1-\alpha_\theta)\,(1 + C_\varepsilon) \tag{B.17}$$

Appendix B.4. AFM

The AFM is obtained using $\alpha_\theta = 1$ in the equations of the EB-AFM. Eqs. (B.11), (B.12) and (B.14) are used, and

$$\overline{u_i'\theta'} = -C_\theta T\left[\overline{u_i'u_j'}\frac{\partial\overline{\theta}}{\partial x_j} + \xi\overline{u_j'\theta'}\frac{\partial\overline{u_i}}{\partial x_j} + \eta\beta g_i\overline{\theta'^2}\right] \tag{B.18}$$

$$C_\theta = \frac{C_\theta'}{C_{1\theta}};\; C_\theta' = 0.98;\; \xi = (1 - C_{2\theta});\; \eta = (1 - C_{3\theta}) \tag{B.19}$$

Appendix B.5. EB-GGDH

The EB-GGDH is obtained from the EB-AFM by applying $\xi = \eta = 0$. Eqs. (B.9), (B.10) (B.11) and (B.16) are used and

$$\overline{u_i'\theta'} = -C_\theta T\left[\overline{u_i'u_j'}\frac{\partial\overline{\theta}}{\partial x_j} + \chi\frac{\varepsilon}{k}\overline{u_j'\theta'}n_in_j\right] \tag{B.20}$$

$$C_\theta' = 0.91; \chi = (1-\alpha_\theta)\,(1 + C_\varepsilon) \tag{B.21}$$

Appendix B.6. GGDH

The GGDH is the EB-GGDH with $\alpha_\theta = 1$, or the AFM with $\xi = \eta = 0$, i.e., Eq. (B.11) is used and

$$\overline{u_i'\theta'} = -C_\theta T\left[\overline{u_i'u_j'}\frac{\partial\overline{\theta}}{\partial x_j}\right] \tag{B.22}$$

$$C_\theta = \frac{C_\theta'}{C_{1\theta}};\; C_\theta' = 0.98 \tag{B.23}$$

References

Abe, H., Kawamura, H., Matsuo, Y., 2004. Surface heat-flux fluctuations in a turbulent channel flow up to $Re_\tau = 1020$ with $Pr = 0.025$ and 0.71. Int. J. Heat Fluid Fl. 25 (3), 404–419.

Archambeau, F., Méchitoua, N., Sakiz, M., 2004. Code Saturne: A Finite Volume Code for the Computation of Turbulent Incompressible flows - Industrial Applications. Int. J. on Finite Volume, Electronical edition: http://averoes.math.univ-paris13.fr/html ISSN 1634 (0655).

Billard, F., Craft, T., Revell, A., 2011. Application of Advanced Reynolds Stress Transport Models to Highly Separated Flows. In: Proc. 7th Int. Symp. Turb. Shear Flow Phenomena, Ottawa, Canada.

Billard, F., Laurence, D., 2012. A robust k-ε-v^2/k elliptic blending turbulence model applied to near-wall, separated and buoyant flows. Int. J. Heat Fluid Fl. 33 (1), 45–58.

Borello, D., Hanjalic, K., Rispoli, F., 2005. Prediction of cascade flows with innovative second-moment closures. J. Fluid Eng.-T. ASME 127 (6), 1059–1070.

Choi, S.-K., Kim, S.-O., 2008. Treatment of turbulent heat fluxes with the elliptic-blending second-moment closure for turbulent natural convection flows. Int. J. Heat Mass Tran. 51 (9–10), 2377–2388.

Daly, B. J., Harlow, F. H., 1970. Transport Equations in Turbulence. Phys. Fluids 13, 2634–2649.

Dehoux, F., 2012. Modélisation statistique des écoulements turbulents en convection forcée, mixte et naturelle. Ph.D. thesis, university of Poitiers.

Dehoux, F., Lecocq, Y., Benhamadouche, S., Manceau, R., Brizzi, L.-E., 2012. Algebraic modeling of the turbulent heat fluxes using the elliptic blending approach. Application to forced and mixed convection regimes. Flow Turbul. Combust. 88 (1), 77–100.

Dol, H., Hanjalić, K., Kenjereš, S., 1997. A comparative assessment of the second-moment differential and algebraic models in turbulent natural convection. Int. J. Heat Fluid Fl. 18 (1), 4–14.

Durbin, P. A., 1991. Near-Wall Turbulence Closure Modeling Without "Damping Functions". Theor. Comput. Fluid Dyn. 3, 1–13.

Flageul, C., Benhamadouche, S., Lamballais, E., Laurence, D., 2015. DNS of turbulent channel flow with conjugate heat transfer: Effect of thermal boundary conditions on the second moments and budgets. Int. J. Heat Fluid Fl. 55, 34–44.

Hanjalić, K., 2002. One-point closure models for buoyancy-driven turbulent flows. Annu. Rev. Fluid Mech. 34, 321–347.

Hanjalić, K., Launder, B., 2011. Modelling Turbulence in Engineering and the Environment. Second-Moment Routes to Closure. Cambridge University Press.

Hanjalić, K., Popovac, M., Hadžiabdić, M., 2004. A robust near-wall elliptic relaxation eddy-viscosity turbulence model for CFD. Int. J. Heat Fluid Fl. 25, 1047–1051.

Howard, R., Serre, E., 2015. Large eddy simulation in Code_Saturne of thermal mixing in a T junction with brass wall. In: Proc. 8th Int. Symp. Turbulence, Heat and Mass Transfer, Sarajevo, Bosnia-Herzegovina.

Kasagi, N., Nishimura, M., 1997. Direct Numerical Simulation of Combined Forced and Natural Turbulent Convection in a Vertical Plane Channel. Int. J. Heat Fluid Fl. 18 (1), 88–99.

Kenjereš, S., Gunarjo, S., Hanjalić, K., 2005. Contribution to elliptic relaxation modelling of turbulent natural and mixed convection. Int. J. Heat Fluid Fl. 26 (4), 569–586.

Launder, B. E., 1988. On the Computation of Convective Heat Transfer in Complex Turbulent Flows. J. Heat Transf. 110, 1112–1128.

Laurence, D. R., Uribe, J. C., Utyuzhnikov, S. V., 2005. A robust formulation of the v2–f model. Flow Turbul. Combust. 73 (3–4), 169–185.

Manceau, R., 2015. Recent progress in the development of the Elliptic Blending Reynolds-stress model. Int. J. Heat Fluid Fl. 51, 195–220.

Manceau, R., Hanjalić, K., 2002. Elliptic Blending Model: A New Near-Wall Reynolds-Stress Turbulence Closure. Phys. Fluids 14 (2), 744–754.

Manceau, R., Parneix, S., Laurence, D., 2000. Turbulent heat transfer predictions using the $\overline{v'v'}$–f model on unstructured meshes. Int. J. Heat Fluid Fl. 21 (3), 320–328.

Manceau, R., Wang, M., Laurence, D., 2001. Inhomogeneity and anisotropy effects on the redistribution term in Reynolds-averaged Navier–Stokes modelling. J. Fluid Mech. 438, 307–338.

Mansour, N. N., Kim, J., Moin, P., 1988. Reynolds-stress and dissipation-rate budgets in a turbulent channel flow. J. Fluid Mech. 194, 15–44.

Menter, F. R., 1994. Two-equation eddy-viscosity turbulence models for engineering applications. AIAA J. 32 (8), 1598–1605.

Parneix, S., Behnia, M., Durbin, P. A., 1998. Predictions of Turbulent Heat Transfer in an Axisymmetric Jet Impinging on a Heated Pedestal. J. Heat Transf. 120, 1–7.

Peeters, T. W. J., Henkes, R. A. W. M., 1992. The Reynolds-stress model of turbulence applied to the natural-convection boundary layer along a heated vertical plate. Int. J. Heat Mass Tran. 35 (2), 403–420.

Pope, S., 2000. Turbulent Flows. Cambridge University Press, New-York.

Shikazono, N., Kasagi, N., 1996. Second-moment closure for turbulent scalar transport at various Prandtl numbers. Int. J. Heat Mass Tran. 39 (14), 2977–2987.

Shin, J. K., An, J. S., Choi, Y. D., Kim, Y. C., Kim, M. S., 2008. Elliptic relaxation second moment closure for the turbulent heat fluxes. J. Turbul. 9 (3), 1–29.

Speziale, C. G., Sarkar, S., Gatski, T. B., 1991. Modeling the pressure-strain correlation of turbulence: an invariant dynamical system approach. J. Fluid Mech. 227, 245–272.

Sveningsson, A., Davidson, L., 2005. Computations of flow field and heat transfer in a stator vane passage using the $\overline{v^2}$–f turbulence model. J. Turbomach. 127 (3), 627–634.

Thielen, L., Hanjalić, K., Jonker, H., Manceau, R., 2005. Predictions of flow and heat transfer in multiple impinging jets with an elliptic-blending second-moment closure. Int. J. Heat Mass Tran. 48 (8), 1583–1598.

Tiselj, I., Bergant, R., Mavko, B., Bajsić, I., Hetsroni, G., 2001. Direct numerical simulation of turbulent heat transfer in channel flow with heat conduction in the solid wall. J. Heat Transf. 123 (5), 849–857.

Trias, F., Soria, M., Oliva, A., Pérez-Segarra, C., 2007. Direct numerical simulations of two- and three-dimensional turbulent natural convection flows in a differentially heated cavity of aspect ratio 4. J. Fluid Mech. 586, 259–293.

Vanpouille, D., Aupoix, B., Laroche, E., 2014. Development of an explicit algebraic turbulence model for buoyant flows – Part 2: Model development and validation. Int. J. Heat Fluid Fl.

Versteegh, T. A. M., Nieuwstadt, F. T. M., 1998. Turbulent budget of natural convection in an infinite, differentially heated, channel flow. Int. J. Heat Fluid Fl. 19, 135–149.

Viti, V., Huang, G., Bradshaw, P., 2007. Numerical study of stress-transport turbulence models: Implementation and validation issues. Comput. Fluids 36 (8), 1373–1383.